J Therm Anal Calorim (2017) 129:1831–1838
DOI 10.1007/s10973-017-6267-7

The reduction mechanism and kinetics of Fe_2O_3 by hydrogen for chemical-looping hydrogen generation

Yidi Wang[1] · **Xinyue Wang**[1] · **Xiuning Hua**[1] · **Chaocheng Zhao**[1] · **Wei Wang**[1]

Received: 21 July 2016 / Accepted: 6 March 2017 / Published online: 23 March 2017

Abstract Low-grade hydrogen-containing gases can be converted into high-value pure hydrogen by chemical-looping hydrogen generation. Iron-based oxygen carrier is believed to be the most suitable oxygen carrier for CLHG. It is essential to investigate the reduction mechanism and kinetics of Fe_2O_3 with hydrogen. The reduction of Fe_2O_3 by H_2 was conducted in a thermogravimetric analyzer at 973–1172 K. The phase analysis of reduction products in different reduction stages illustrated that $Fe_2O_3 \rightarrow Fe_3O_4$ and $Fe_3O_4 \rightarrow FeO$ proceed simultaneously; hence, the reduction process is a two-step reaction, in the sequence of $Fe_2O_3 \rightarrow FeO$ and $FeO \rightarrow Fe$. To investigate the reaction mechanisms for the two steps, the Hancock–Sharp method and the nonlinear fitting approach were applied to select the kinetic models. The reaction mechanisms of $Fe_2O_3 \rightarrow FeO$ can be described by nucleation and growth model. The activation energy is 36.74 ± 1.09 kJ mol^{-1}, and reaction rate equation derived from Arrhenius law is estimated for $Fe_2O_3 \rightarrow FeO$. As for $FeO \rightarrow Fe$, the first stage is controlled by the phase-boundary reaction, and the oxygen diffusion affects the last stage of the reduction process.

Keywords Chemical-looping hydrogen generation · Hydrogen · Iron oxide · Kinetic model · Reaction mechanism

Introduction

Climate change and energy shortage represent an urgent and potentially irreversible threat to human society. China's energy utilization efficiency is far lower than the Europe and other developed countries [1], and China needs to further reduce carbon dioxide emissions per unit of gross domestic product [2]. High-purity hydrogen is in great demand at hydrogenation process and fuel cell to meet the increasingly stringent requirements of environmental requirements in China [3, 4]. Chemical-looping hydrogen generation (CLHG) is developed from both chemical-looping combustion (CLC) and hydrogen production by the steam–iron process. CLHG produces high-purity hydrogen while achieving low-cost inherent CO_2 separation [5]. In addition, low NO_X [6] and low dioxin [7] are realized by avoiding direct contact between fuel and gaseous oxygen for CLHG.

The reduction of iron-based oxygen carriers is the key part of the entire cycle. Steam–iron process only occurred between steam and either Fe or FeO. And the hydrogen production potential positively correlates with the reduction degree of the iron oxides. So the study on deep reduction of iron oxides necessitates an improved understanding of reduction mechanisms and determination of the kinetic parameters for reduction processes [8–10]. Synthesis gas from biomass pyrolysis or coal gasification and refinery gas can be used as fuel gases in the CLC process [11]. Although the concentration of H_2 in hydrogen-containing gas is about 5–20% in the low-temperature pyrolysis or other conventional technology with the goal of producing bio-char or bio-oil, the hydrogen-rich gas through high reaction temperature, high heating rate and the catalyst has attracted more and more attentions [12–14]. The concentration gradient of H_2 in this work

✉ Wei Wang
solid@tsinghua.edu.cn

[1] School of Environment, Tsinghua University, Beijing 100084, China

(10–40%) was chosen on the basis of generalized hydrogen-containing gas and hydrogen-rich gas. By CLHG, low-grade hydrogen-containing gases can be converted into high-value pure hydrogen.

Actually adding some inert supports or poly-metallic structure would improve or inhibit the reactivity and stability over cycling [15–17]. This could be because the compound in inert support may catalyze the reduction reaction, or the compound in inert support may react with Fe_2O_3. Luo et al. [18] investigated the performance of three iron-based oxygen carriers (pure Fe_2O_3, synthetic $Fe_2O_3/MgAl_2O_4$ and iron ore) in reduction process using methane as fuel. They found that iron-based mixed oxygen carrier particles were potential to be used in methane chemical-looping process, but the reactivity of the iron ore needs to be increased. Hua et al. [19] found Fe_2O_3/Al_2O_3 showed better reactivity and higher activation energy than pure Fe_2O_3 by comparing the reduction mechanism and kinetics of pure Fe_2O_3 and Fe_2O_3/Al_2O_3. It is clear that the reduction kinetics and mechanism of pure Fe_2O_3 are fundamental and essential to understand the reduction behavior of various iron-based oxygen carriers.

Although the reduction of iron-based oxygen carrier by CO and H_2–CO mixtures has been extensively studied [19–21], the study on reduction kinetics of iron-based oxygen carrier by H_2 at different concentrations is relatively limited. Lin et al. [22] studied the two-stage reduction of iron oxide by hydrogen and proposed a unimolecular model for $Fe_2O_3 \rightarrow Fe_3O_4$ and a 2D nucleation model for $Fe_3O_4 \rightarrow Fe$. Sastri et al. [23] proposed the reduction of Fe_2O_3 by hydrogen proceeded by a consecutive two-step mechanism via Fe_3O_4. Moon et al. [24] investigated the reduction behavior of hematite by H_2 and H_2–CO mixtures. The reduction is controlled by the chemical reaction at oxide/metal interface initially, mixed controlled in the transition phase and followed by the diffusion control toward the end of the reduction. Zhou et al. [25] used the Johnson–Mehl–Avrami kinetic model to study the reduction of hematite to Fe by pure hydrogen at 873–1073 K. Bonalde et al. [26] studied the reduction kinetics of hematite pellets by H_2–CO mixture. They proposed that the chemical reaction and internal gas diffusion are competing processes during the first stage of the reduction and that internal gas diffusion is the controlling step at the last stage of the process. Pineau et al. [27] proposed that the reduction of $Fe_2O_3 \rightarrow Fe_3O_4$ by H_2 is characterized by an apparent activation energy of 76 kJ mol^{-1}. The apparent activation energy of $Fe_3O_4 \rightarrow Fe$ is 88 and 39 kJ mol^{-1} for temperatures lower and higher than 693 K, respectively. In summary, in a reaction with CO and H_2, the reduction of Fe_2O_3 is usually described as a two-step mechanism, i.e., $Fe_2O_3 \rightarrow Fe_3O_4 \rightarrow Fe$ or $Fe_2O_3 \rightarrow FeO \rightarrow Fe$ [28].

The reduction behavior and mechanism of iron-based oxygen carriers are still not well understood, and there has been considerable disagreement in kinetic data mentioned above. This study aims to explore the mechanism reactions between pure Fe_2O_3 and H_2 with the assistance of X-ray diffraction analysis. Moreover, most works before were only successful in obtaining independent equations for specific reducing condition. This study aims to develop a theoretical rate equation for specific concentration gradient of H_2.

Experimental

Preparation of iron-based oxygen carrier

Pure Fe_2O_3 powder (analytical reagent, Sinopharm Chemical Reagent Co., Ltd., China) was calcined at 1473 K for 24 h and was sieved to a uniform size of 100–200 μm.

Experiment procedure

Kinetic data were obtained in a thermogravimetric analyzer (TA-STD 600, TA Instruments Inc., USA) under isothermal conditions. The gas flow of reducing gases was controlled by an external mass flow controller and was diluted by N_2 before being introduced into the TG. Iron-based oxygen carrier particles (40 mg) were placed in an aluminum oxide crucible and then heated from ambient temperature to designed temperatures (973–1173 K) under N_2 atmosphere. 10–40% H_2 balanced by N_2 was introduced to TG. The volume flow of the H_2/N_2 mixtures was 100 mL min^{-1}. The reaction finished when mass losing rate dropped to nearly 0.01 mg s^{-1}.

The iron-based oxygen carriers with mass ratios of 0.97, 0.90 and 0.89 described in Fig. 1 are reduction products of initial Fe_2O_3. To understand the transformation of iron oxides in the reduction process, the mass of sample was shown on the TG in real time, and the reactant gases were converted from reducing gases to inert gas when the mass ratios reached the objective ones of 0.97, 0.90 and 0.89, respectively.

The phase structure of the iron oxides was identified with X-ray diffraction (XRD, D8 Advance, Bruker Inc., Germany) with the use of Cu Kα1 (40 kV, 40 mA, $\lambda = 0.15406$ nm). The samples were scanned at a rate of 6° min^{-1} from $2\theta = 20°–90°$. The qualitative phase analysis was solved by the XRD analysis software Jade (v9.3, Materials Data, Inc., USA).

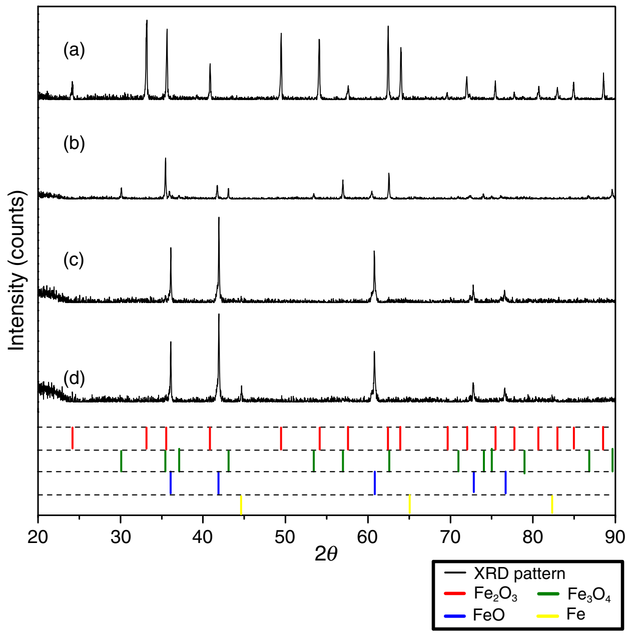

Fig. 1 XRD patterns of iron-based oxygen carrier with specific at 1173 K: (*a*) initial iron-based oxygen carrier; (*b–d*) iron-based oxygen carriers with mass ratios of 0.97, 0.90 and 0.89

Kinetic model

In general, the kinetic model of a gas–solid reaction can be expressed as follows:

$$\frac{dX}{dt} = kf(X) \tag{1}$$

The integral of Eq. (1) was obtained as follows:

$$g(X) = \int_0^X \frac{dX}{f(X)} = kt \tag{2}$$

where dX/dt is the solid conversion rate; X is the solid conversion; t is the reaction time, *s*; and k is the reaction rate constant which satisfies the Arrhenius law:

$$k = k_0 e^{-\frac{E_a}{RT}} \tag{3}$$

which can also be written as:

$$\ln k = \ln k_0 + \left(-\frac{E_a}{R}\right)\frac{1}{T} \tag{4}$$

where k_0 is the pre-exponential factor; E_a is the activation energy, kJ mol^{-1}; R is the ideal gas constant, 8.314 J mol^{-1} K^{-1}; T is the absolute temperature, K. The activation energy and pre-exponential factor can be calculated by plotting $\ln k - 1/T$.

The models, which typically interpret the reaction mechanism for the solid–gas reaction of iron oxides, are commonly categorized as reaction order (*F*), geometrical contraction (*R*), diffusion (*D*), and nucleation (Avrami–Erofe'ev, AE). The expressions of $f(X)$ and $g(X)$ of the kinetic models are listed in Table 1.

Hancock and Sharp developed a simplified solution to improve the efficiency of the screening reaction model. The expression is as follows:

$$X(t) = 1 - e^{-at^n} \tag{5}$$

which can be written as:

$$\ln(-\ln(1 - X(t))) = \ln a + n \ln t \tag{6}$$

where a is a constant that partially depends on the nucleation frequency of nuclei formation and the rate of crystalline growth; n is a constant associated with the geometric shape of particles. Slope n can be used as a diagnostic tool by plotting $\ln(\ln(1 - X)) - \ln t$ to preliminarily screen all types of kinetic mechanisms in Table 1. Those kinetic mechanisms whose n are approximate to the slope n are regarded as the candidate mechanisms.

The Hancock–Sharp method, which is based on the nucleation and nuclei growth model, is commonly used at the solid conversion ranging from 0.15 to 0.5. Selecting the best fit model by plotting $X - t$ over a full-scale range is preferable. That is, the kinetic expressions of the candidate models are utilized to match the experimental data in the form of $X - t$ profiles, and models with the smallest residual sum of squares (RSS) and Akaike information criterion with correction (AIC_C) are selected among the candidate mechanisms mentioned above [31]. The parameter estimation program was solved using multivariable least-squares regression in MATLAB (R2015b, Mathworks Inc., USA).

Results and discussion

Characteristics of iron-based oxygen carriers

The initial iron-based oxygen carrier was pure Fe_2O_3, and the X-ray diffraction pattern of this oxygen carrier is shown in Fig. 1a. In theory, the $Fe_2O_3 \rightarrow Fe_3O_4$ will loss 3.34% mass of pure Fe_2O_3; the $Fe_2O_3 \rightarrow FeO$ will loss 10% mass of pure Fe_2O_3. The mass ratios 0.966 and 0.90 are associated with mass loss of producing Fe_3O_4 and FeO, respectively. The iron-based oxygen carrier with a mass ratios of 0.97 consists of Fe_3O_4, FeO and Fe_2O_3 and devoid of Fe as in Fig. 1b. The existence of FeO indicated that the $Fe_2O_3 \rightarrow Fe_3O_4$ and $Fe_3O_4 \rightarrow FeO$ both conducted in the mass loss stage from 1 to 0.97. The iron-based oxygen carrier with a mass ratios of 0.90 consists of mainly FeO and slightly Fe_3O_4 and devoid of Fe_2O_3 and Fe as in Fig. 1c. This indicated that FeO → Fe did not conduct in the mass loss stage from 1 to 0.90. The iron-based oxygen carrier with a mass ratios of 0.89 consists of FeO and Fe

Table 1 Rate and integral expressions for common gas–solid reactions [29, 30]

No.	Reaction mechanism	$f(X) = 1/k\ dX/dt$	$g(X) = kt$	n
F0 (R1)	Zero-order or phase-boundary controlled	1	X	1.24
F1 (AE1)	First-order or one-dimensional growth of nuclei	$(1 - X)$	$-\ln(1 - X)$	1
F1.5	Three-halves order	$(1 - X)^{1.5}$	$2[(1 - X)^{(-1/2)} - 1]9$	0.91
F2	Second-order	$(1 - X)^2$	$(1 - X)^{-1} - 1$	0.83
R2	Phase-boundary controlled	$2(1 - X)^{1/2}$	$1-(1 - X)^{1/2}$	1.11
R3	Phase-boundary controlled	$3(1 - X)^{2/3}$	$1-(1 - X)^{1/3}$	1.07
D1	One-dimensional diffusion	$1/(2X)$	X^2	0.62
D2	Two-dimensional diffusion	$1/[-\ln(1 - X)]$	$(1 - X)\ln(1 - X) + X$	0.57
D3	Three-dimensional diffusion	$3(1 - X)^{(1/3)}/[2(1 - X)^{(-1/3)} - 1]$	$[1-(1 - X)^{(1/3)}]^2$	0.54
AE1.5	Avrami–Erofe'ev ($n = 1.5$)	$3/2(1 - X)[-\ln(1 - X)]^{1/3}$	$[-\ln(1 - X)]^{2/3}$	1.5
AE2	Avrami–Erofe'ev ($n = 2$)	$2(1 - X)[-\ln(1 - X)]^{1/2}$	$[-\ln(1 - X)]^{1/2}$	2
AE3	Avrami–Erofe'ev ($n = 3$)	$3(1 - X)[-\ln(1 - X)]^{2/3}$	$[-\ln(1 - X)]^{1/3}$	3
AEn	Avrami–Erofe'ev	$4(1 - X)[-\ln(1 - X)]^{(n-1)/n}$	$[-\ln(1 - X)]^{1/n}$	n

and devoid of Fe_2O_3 and Fe_3O_4 as in Fig. 1d. This indicated that $Fe_2O_3 \rightarrow Fe_3O_4$ and $Fe_3O_4 \rightarrow FeO$ did not conduct in the mass loss stage from 0.90 to 0.70. The results illustrated that $Fe_2O_3 \rightarrow Fe_3O_4$ and $Fe_3O_4 \rightarrow FeO$ proceeded simultaneously. But $Fe_2O_3 \rightarrow FeO$ and $FeO \rightarrow Fe$ proceeded independently because there is no Fe coexisted with Fe_2O_3 or Fe_3O_4.

Reduction performance and reduction kinetics of iron oxides

The reduction performance of Fe_2O_3 reduced by 40% H_2 at different temperatures is shown in Fig. 2. Figure 2 shows that the reaction rates of mass loss increase significantly with temperature in each step. It is also seen that the mass loss at the first stage of the reduction ($m(t)/m_0 = 1$–0.9) was fast, and then, the reduction slowed in the middle of the reduction ($m(t)/m_0 = 0.9$–0.8). At the last stage of the reduction ($m(t)/m_0 = 0.8$–0.7), the mass loss became slower than other before. On the basis of the phase analysis with different mass ratios, two intermediate reactions ($Fe_2O_3 \rightarrow FeO$ and $FeO \rightarrow Fe$) were relatively

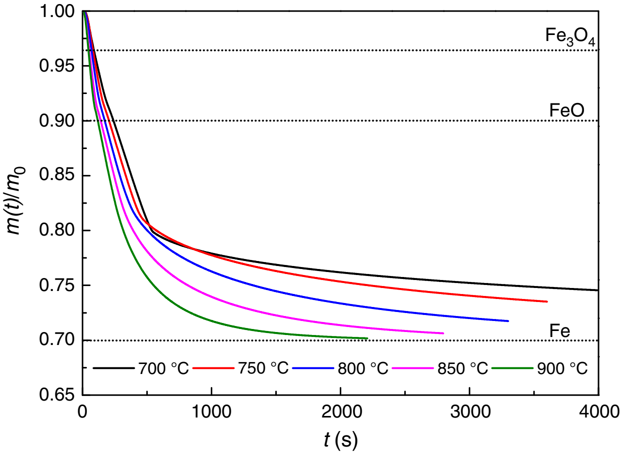

Fig. 2 Mass changing curve of reduction with 40% H_2

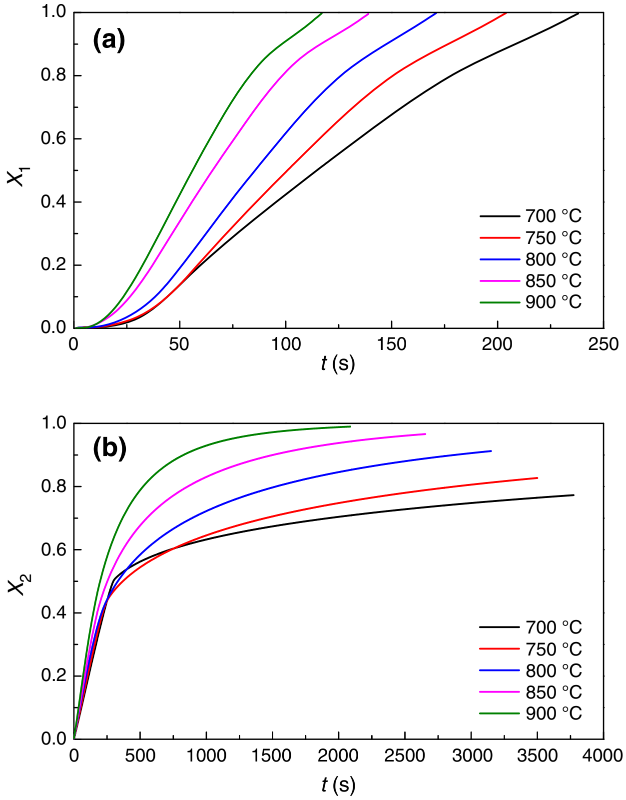

Fig. 3 $X - t$ plots of two steps at different temperatures with 40% H_2: **a** $Fe_2O_3 \rightarrow FeO$, **b** $FeO \rightarrow Fe$

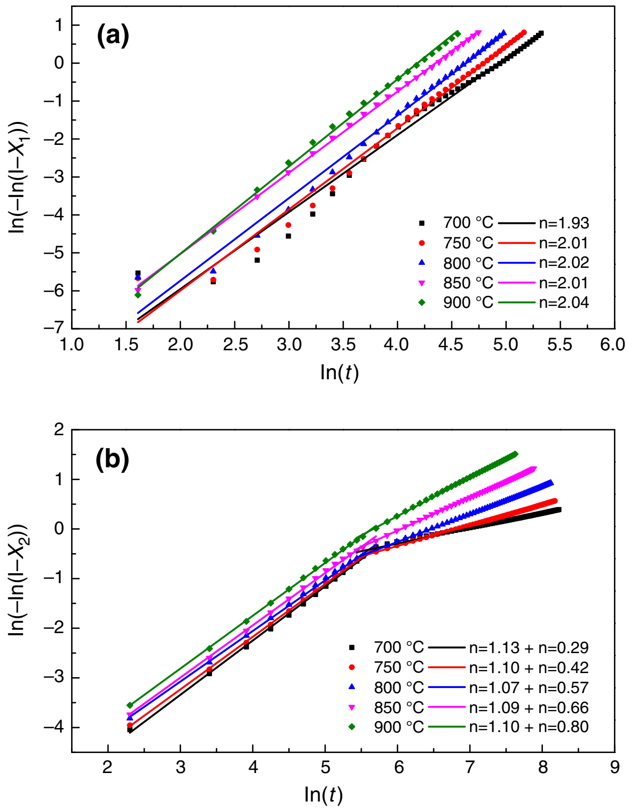

Fig. 4 Plots of the Hancock and Sharp method for two steps with 40% H_2: **a** Fe_2O_3 → FeO, **b** FeO → Fe

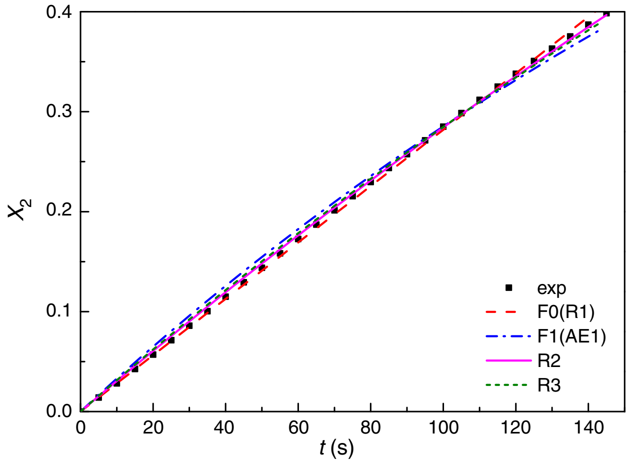

Fig. 5 Comparison between the experimental data of the $X - t$ and model predictions with 40% H_2 at 1173 K for FeO → Fe

independent at 973–1173 K; thus, the mass loss may proceed according to the following reactions:

$$Fe_2O_3 + H_2 = 2FeO + H_2O \quad (7)$$

$$FeO + H_2 = Fe + H_2O. \quad (8)$$

Table 2 Statistical analyses of the candidate models for the $X - t$

Model	900 °C	
	RSS	AIC_C
F0 (R1)	19.03×10^{-3}	−202.7
F1 (AE1)	38.19×10^{-4}	−250.9
R2	24.50×10^{-4}	−264.2
R3	61.86×10^{-4}	−236.4

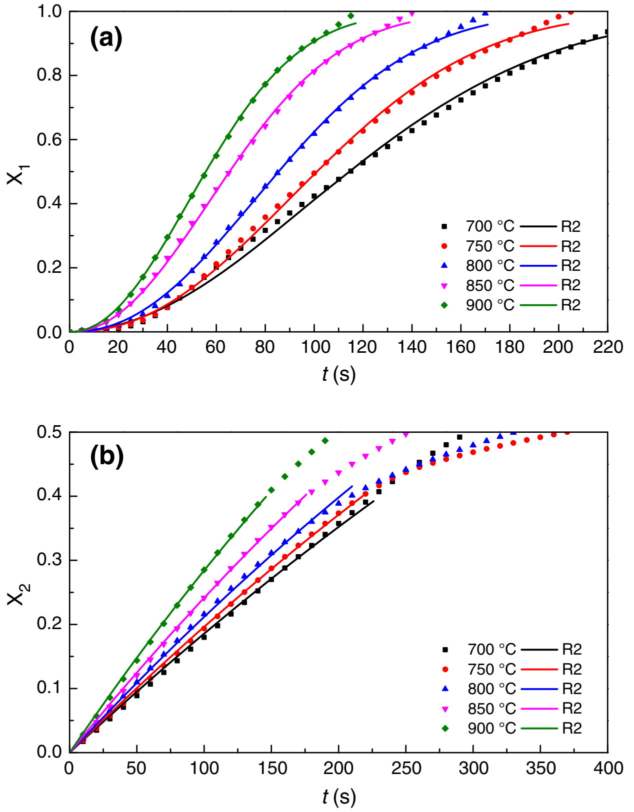

Fig. 6 Comparison of experimental data with calculation results with 40% H_2: **a** Fe_2O_3 → FeO, **b** first section of FeO → Fe

On the basis of the stoichiometry of the reduction of Fe_2O_3, the mass changes of Eqs. 7 and 8 correspond to 10 and 20% of the initial sample. Thus, the solid conversion for each step can be defined as follows:

$$X_i(t) = \frac{(m_{i,0} - m(t))}{m_0 \times X_i^*} \quad (i = 1, 2), \quad (9)$$

where $m_{i,o}$ is the initial mass of iron-based oxygen carriers in the step i, mg; $m(t)$ is the mass of iron-based oxygen carriers at time t, mg; m_0 is the initial mass of iron-based oxygen carriers, mg; and X_i* is the solid conversion of step i in theory, with $X_1* = 0.1$, $X_2* = 0.2$.

Figure 3 indicates the $X - t$ of the two steps is calculated by Eq. (9). The reaction rate of Fe_2O_3 → FeO grew at the beginning and declined at the end. The process of

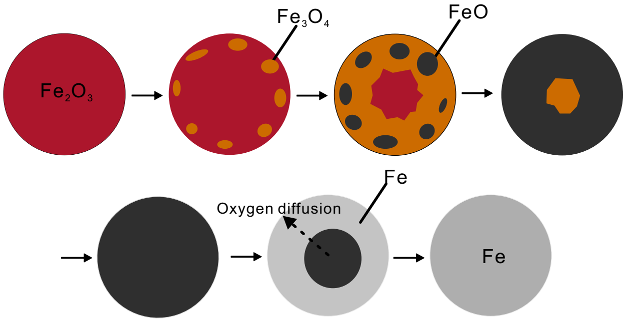

Fig. 7 Scheme of nuclei growth model and geometrical contracting model and nucleation applicable to iron oxides crystallite

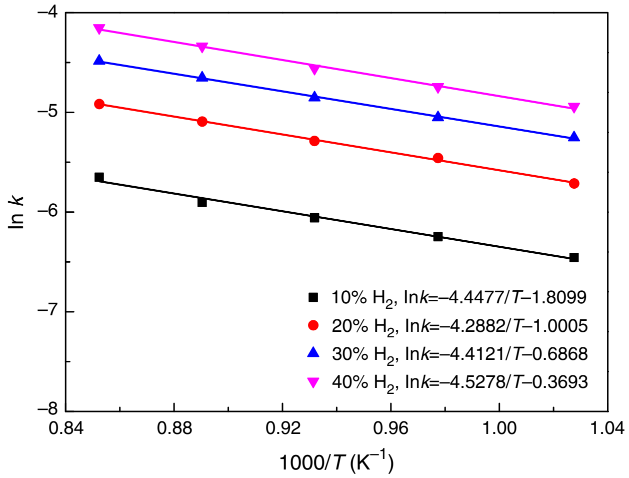

Fig. 8 Arrhenius plots of Fe_2O_3 → FeO

FeO → Fe can be divided into two stages. The reaction rate FeO → Fe was relatively fast at the first stage ($X_2 = 0$–0.4) and become slow at the last stage ($X_2 = 0.4$–1).

To determine the reaction mechanism of each step, the Hancock and Sharp method was applied. The $\ln(\ln(1-X)) - \ln t$ plots and corresponding n values are illustrated in Fig. 4. The slopes for Fe_2O_3 → FeO are in the range of 2 ± 0.1. These results indicate that this step is isokinetic within the temperature range 973–1173 K; that is, the mechanism is the same for various H_2 concentrations and different temperatures. As for FeO → Fe, the plots of $\ln(\ln(1-X)) - \ln t$ consisted of two stages. The slopes of first section are in the range of 1.10 ± 0.1, whereas those of the second section increase with temperature. The reaction mechanism of Fe_2O_3 → FeO can be described by the nucleation and growth model AE2 (i.e., Avrami–Erofe'ev equation). The n values of the first section of FeO → Fe are in the range of 1.0–1.2, which identify F0 ($n = 1.24$), F1 ($n = 1$), R2 ($n = 1.11$) and R3 ($n = 1.07$) as the substantive kinetic models. Figure 5 shows the comparison between the experimental data and the model predictions of the four substantive models, with 40% H_2 at 1173 K. The regression statistics of the four models are listed in Table 2.

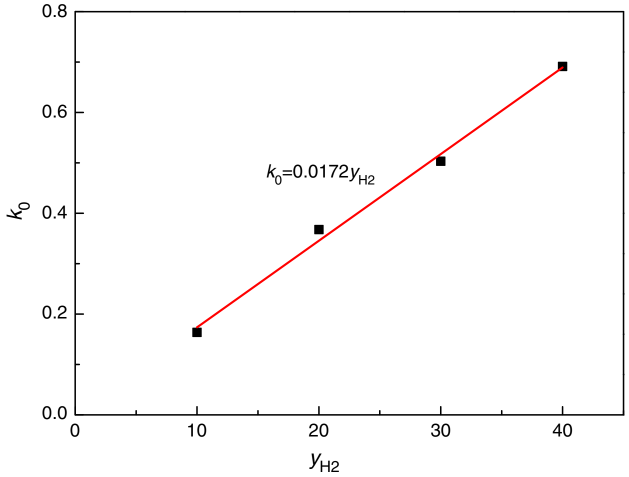

Fig. 9 Effect of H_2 concentration on the reaction rate constant for Fe_2O_3 → FeO

The results of the $X - t$ fitting show that R2 exhibits the smallest RSS and AIC_C than other models. The fitting results indicate that R2 is the most suitable mechanism for the first section of FeO → Fe.

The comparisons of the experimental data with the calculation results from AE2 and R2 are shown in Fig. 6. For Fe_2O_3 → FeO, the AE2 model predicts the experimental data very well. As for FeO → Fe, the first section is controlled by a phase-boundary reaction. Then, the chemical reaction and oxygen diffusion are competing processes during the transition stage, and oxygen diffusion is the controlling step at the last stage.

Figure 7 presents the schematic description of two steps. The crystalline grains of Fe_3O_4 proceed with nucleation and growth on the surface of Fe_2O_3 particle. Before all Fe_2O_3 transforms into Fe_3O_4, the crystalline grains of FeO appear on the surface of iron-based oxygen carrier particle. Then, crystalline grains of FeO grow and the particle becomes pure FeO. The first section of FeO → Fe is controlled by geometrical contraction models. The geometrical contraction models in Table 1 are form of the classic shrinking core model with the phase-boundary reaction control of different geometries. The R2 model represents 2D growth/shrinkage. At the last stage of FeO → Fe, the rate is controlled by oxygen diffusion, that is, the transport of oxygen to the active interface [32].

The rate equation for Fe_2O_3 → FeO is given as:

$$(-\ln(1-X))^{1/2} = kt \tag{10}$$

The reaction rate k at different temperatures and CO concentrations can be obtained by Eq. (10). The activation energy together with the pre-exponential factor is obtained from the Arrhenius equation. The resulting activation energy was determined from the slope of the lines in Fig. 8, whereas the values of the intercept are the pre-exponential factor. The activation energy of $Fe_2O_3 \rightarrow FeO$ was estimated to be 36.74 ± 1.09 kJ mol^{-1}. The value of k_0 increased with increasing H_2 concentration in the same step. As shown in Fig. 9, a significant linear correlation can be observed between the pre-exponential factors and the H_2 concentrations. Combining the equations in Fig. 9, the reaction rates constant derived from the Arrhenius equation for $Fe_2O_3 \rightarrow FeO$ can be estimated as follows:

$$k_1\left(\mathrm{s}^{-1}\right) = 0.0172 y_{H_2} \mathrm{e}^{-\frac{4418.95}{T}} \tag{11}$$

where k_1 is the chemical reaction rate for $Fe_2O_3 \rightarrow FeO$; y_{H2} is the H_2 concentration.

The reaction rate equation for $Fe_2O_3 \rightarrow FeO$ is as follows:

$$\begin{aligned}\frac{\mathrm{d}X_1}{\mathrm{d}t} &= k_1 f(X) \\ &= 0.0172 y_{H_2} \mathrm{e}^{-\frac{4418.95}{T}} \times 2 \times (1 - X_1) \times [-\ln(1 - X)]^{1/2}\end{aligned} \tag{12}$$

where $\mathrm{d}X_1/\mathrm{d}t$ is the chemical reaction rate for $Fe_2O_3 \rightarrow FeO$; X_1 is the solid conversion for $Fe_2O_3 \rightarrow FeO$.

Conclusions

XRD patterns illustrate that $Fe_2O_3 \rightarrow Fe_3O_4$ and $Fe_3O_4 \rightarrow FeO$ proceed simultaneously. The reduction of Fe_2O_3 by H_2 is a two-step process, i.e., $Fe_2O_3 \rightarrow FeO$ and $FeO \rightarrow Fe$. The $Fe_2O_3 \rightarrow FeO$ is controlled by 2D nucleation and growth model, and its activation energy is estimated to be 36.74 ± 1.09 kJ mol^{-1}. A theoretical rate equation is developed to predict the reaction rate in the process of $Fe_2O_3 \rightarrow FeO$ with 10–40% H_2. As for $FeO \rightarrow Fe$, the kinetic mechanisms varied between three reaction stages: the first stage is controlled by 2D phase-boundary model; chemical reaction and oxygen diffusion are competing processes during the transition stage; then, oxygen diffusion is the controlling step at the last stage of the process. The study on reduction mechanism and kinetics of pure Fe_2O_3 by hydrogen is essential for the exploration on deep reduction for CLHG and provides fundamental data for the evaluation and selection of iron-based oxygen carriers.

Acknowledgements This work was supported by the National Key Technology R&D Program of China (2015BAD21B05 and 2014BAC24B00) and the National Natural Science Foundation of China (Grant No. 21477061). The authors also wish to express thanks to the Beijing Engineering Research Center of Biogas Centralized Utilization (Tsinghua University) for support of the experimental unit construction.

References

1. Crompton P, Wu Y. Energy consumption in China: past trends and future directions. Energy Econ. 2005;27(1):195–208.
2. Yi WJ, Zou LL, Jie G, Kai W, Wei YM. How can China reach its CO_2 intensity reduction targets by 2020? a regional allocation based on equity and development. Energy Policy. 2011;39(5):2407–15.
3. Ben H, Mu W, Deng Y, Ragauskas AJ. Production of renewable gasoline from aqueous phase hydrogenation of lignin pyrolysis oil. Fuel. 2013;103:1148–53.
4. Eberle U, Müller B, von Helmolt R. Fuel cell electric vehicles and hydrogen infrastructure: status 2012. Energy Environ Sci. 2012;5(10):8780–98.
5. Zhang F, Zhao P, Niu M, Maddy J. The survey of key technologies in hydrogen energy storage. Int J Hydrog Energy. 2016;41(33):14535–52.
6. Ishida M, Jin H. A novel chemical-looping combustor without NO_x formation. Ind Eng Chem Res. 1996;35(7):2469–72.
7. Hua X, Wang W. Chemical looping combustion: a new low-dioxin energy conversion technology. J Environ Sci. 2015;32: 135–45.
8. Iliuta I, Tahoces R, Patience GS, Rifflart S, Luck F. Chemical-looping combustion process: kinetics and mathematical modeling. AIChE J. 2010;56(4):1063–79.
9. Zhou Z, Han L, Bollas GM. Model-based analysis of bench-scale fixed-bed units for chemical-looping combustion. Chem Eng J. 2013;233(11):331–48.
10. Zhou Z, Han L, Nordness O, Bollas GM. Continuous regime of chemical-looping combustion (CLC) and chemical-looping with oxygen uncoupling (CLOU) reactivity of CuO oxygen carriers. Appl Catal B. 2015;166:132–44.
11. Forero C, Gayán P, De Diego L, Abad A, García-Labiano F, Adánez J. Syngas combustion in a 500 W th chemical-looping combustion system using an impregnated Cu-based oxygen carrier. Fuel Process Technol. 2009;90(12):1471–9.
12. Inguanzo M, Domínguez A, Menéndez JA, Blanco CG, Pis JJ. On the pyrolysis of sewage sludge: the influence of pyrolysis conditions on solid, liquid and gas fractions. J Anal Appl Pyrolysis. 2002;63(1):209–22.
13. Remón J, Broust F, Valette J, Chhiti Y, Alava I, Fernandez-Akarregi AR, et al. Production of a hydrogen-rich gas from fast pyrolysis bio-oils: comparison between homogeneous and catalytic steam reforming routes. Int J Hydrog Energy. 2014;39(1):171–82.
14. Bridgwater AV. Review of fast pyrolysis of biomass and product upgrading. Biomass Bioenergy. 2012;38:68–94.
15. Abad A, Adánez J, Cuadrat A, García-Labiano F, Gayán P, Luis F. Kinetics of redox reactions of ilmenite for chemical-looping combustion. Chem Eng Sci. 2011;66(4):689–702.
16. Zhao H-Y, Cao Y, Orndorff W, Pan W-P. Study on modification of Cu-based oxygen carrier for chemical looping combustion. J Therm Anal Calorim. 2013;113(3):1123–8.
17. Leion H, Jerndal E, Steenari B-M, Hermansson S, Israelsson M, Jansson E, et al. Solid fuels in chemical-looping combustion using oxide scale and unprocessed iron ore as oxygen carriers. Fuel. 2009;88(10):1945–54.
18. Luo M, Wang S, Wang L, Lv M. Reduction kinetics of iron-based oxygen carriers using methane for chemical-looping combustion. J Power Sources. 2014;270(4):434–40.
19. Hua X, Wang W, Wang F. Performance and kinetics of iron-based oxygen carriers reduced by carbon monoxide for chemical looping combustion. Front Environ Sci Eng. 2015;9(6):1130–8.
20. Monazam ER, Breault RW, Siriwardane R. Reduction of hematite (Fe_2O_3) to wüstite (FeO) by carbon monoxide (CO) for chemical looping combustion. Chem Eng J. 2014;242(242): 204–10.

21. Piotrowski K, Mondal K, Lorethova H, Stonawski L, Szymański T, Wiltowski T. Effect of gas composition on the kinetics of iron oxide reduction in a hydrogen production process. Int J Hydrog Energy. 2005;30(15):1543–54.
22. Lin HY, Chen YW, Li C. The mechanism of reduction of iron oxide by hydrogen. Thermochim Acta. 2003;400(1–2):61–7.
23. Sastri M, Viswanath R, Viswanathan B. Studies on the reduction of iron oxide with hydrogen. Int J Hydrog Energy. 1982;7(12):951–5.
24. Moon I-J, Rhee C-H, Min D-J. Reduction of hematite compacts by H_2–CO gas mixtures. Steel Res. 1998;69(8):302–6.
25. Zhou A, Suzuki K, Sahajwalla V, Cadogan JM. A Mossbauer study of the gas-based direct reduction of iron ore fines and application of the Johnson–Mehl–Avrami kinetic model to the reduction process. Scand J Metall. 1999;28(2):65–9.
26. Bonalde A, Henriquez A, Manrique M. Kinetic analysis of the iron oxide reduction using hydrogen–carbon monoxide mixtures as reducing agent. ISIJ Int. 2005;45(9):1255–60.
27. Pineau A, Kanari N, Gaballah I. Kinetics of reduction of iron oxides by H_2: part I: low temperature reduction of hematite. Thermochim Acta. 2006;447(1):89–100.
28. Slagtern Å, Swaan HM, Olsbye U, Dahl IM, Mirodatos C. Catalytic partial oxidation of methane over Ni-, Co- and Fe-based catalysts. Catal Today. 1998;46(2):107–15.
29. Perrenot B, Widmann G. TG and DSC kinetics of thermal decomposition and crystallization processes. J Therm Anal Calorim. 1991;37(8):1785–92.
30. Wiltowski T, Hinckley CC, Smith GV, Nishizawa T, Saporoschenko M, Shiley RH, et al. Kinetics and mechanisms of iron sulfide reductions in hydrogen and in carbon monoxide. J Solid State Chem. 1987;71(1):95–102.
31. Zhou Z, Han L, Bollas GM. Kinetics of NiO reduction by H_2 and Ni oxidation at conditions relevant to chemical-looping combustion and reforming. Int J Hydrog Energy. 2014;39(16):8535–56.
32. Monazam ER, Breault RW, Siriwardane R. Kinetics of hematite to wüstite by hydrogen for chemical looping combustion. Energy Fuels. 2014;28(8):5406–14.